ÓPTICA PURA Y APLICADA
www.sedoptica.es

Type: RESEARCH PAPER
Section: VISION

Design and Evaluation of the Spiral Optical Element as a Diffractive Element with Extended Depth of Focus for Presbyopia Correction

Diseño y Evaluación del Elemento Óptico Espiral como un Elemento Difractivo con Profundidad de Foco Extendida para la Corrección de la Presbicia

Salomé Osorio-Muñoz,[*1] Walter Torres-Sepúlveda[1,2] and Alejandro Mira-Agudelo[1]

1. Grupo de Óptica y Fotónica, Instituto de Física, Facultad de Ciencias Exactas y Naturales, Universidad de Antioquia UdeA, Calle 70 No. 52-21, Medellín, Colombia.

2. Área de Ciencias Básicas, Grupo de Investigación en Innovación Digital y Desarrollo Social (INDDES), Facultad de Ciencias y Humanidades, Institución Universitaria Digital de Antioquia, Medellín, Colombia.

(*) E-mail: salome.osoriom@udea.edu.co S: miembro de SEDOPTICA / SEDOPTICA member

Received: 18/6/1015 Accepted: 9/12/2025
DOI: 10.7149/OPA.58.4.51219

ABSTRACT:

This study introduces and assesses the Spiral Optical Element (SOE), a novel diffractive optical design intended to provide extended depth of focus (EDOF) for the correction of presbyopia. The SOE's optical performance was evaluated through a combination of computational simulations, optical bench testing, and psychophysical measurements involving five participants. Evaluations were conducted using a monocular visual simulator equipped with a spatial light modulator, an electro-optical lens, and a polychromatic stimulus pathway. Results demonstrate that the SOE yields two peaks in visual acuity at 0 D and −2 D, while maintaining acceptable performance across higher defocus levels. Although the SOE offers a narrower focus range than other similar optical elements, such as the Light Sword Lens (LSL), its consistent optical behavior across test stages supports its potential application as an advanced EDOF solution for presbyopia correction.

Key words: Spiral Optical Element, Diffractive Optical Elements, Presbyopia, Depth of Focus.

RESUMEN:

Este estudio presenta y evalúa el Elemento Óptico Espiral (SOE), un nuevo diseño óptico difractivo que proporciona una profundidad de foco extendida (EDOF) para la corrección de la presbicia. El rendimiento óptico del SOE se evaluó mediante una combinación de simulaciones computacionales, pruebas ópticas en banco y mediciones psicofísicas con cinco participantes. Las pruebas se realizaron utilizando un simulador visual monocular equipado con un modulador espacial de luz, una lente electroóptica y un camino de estímulos policromáticos. Los resultados demuestran que el SOE alcanza dos picos de agudeza visual a 0 D y -2 D, manteniendo un rendimiento aceptable en niveles de desenfoque más altos. Si bien el SOE ofrece un rango de enfoque más estrecho que otros elementos ópticos similares, como la Lente Espada de Luz (LSL), su comportamiento óptico consistente en las distintas etapas de prueba respalda su posible aplicación como una solución EDOF avanzada para la corrección de la presbicia.

Palabras clave: Elemento Óptico Espiral, Elementos Ópticos Difractivos, Presbicia, Profundidad De Foco.

REFERENCES AND LINKS / REFERENCIAS Y ENLACES

[1] T. R. Fricke, N. Tahhan, S. Resnikoff, E. Papas, A. Burnett, S. M. Ho, et al., "Global prevalence of presbyopia and vision impairment from uncorrected presbyopia: systematic review, meta-analysis, and modelling," Ophthalmology **125**(10), 1492–1499 (2018).

[2] J. S. Wolffsohn, L. N. Davies, "Presbyopia: effectiveness of correction strategies," Prog. Retin. Eye Res. **68**, 124–143 (2019).

[3] W. N. Charman, "Developments in the correction of presbyopia I: spectacle and contact lenses," Ophthalmic Physiol. Opt. **34**(1), 8–29 (2014).

[4] W. N. Charman, "Developments in the correction of presbyopia II: surgical approaches," Ophthalmic Physiol. Opt. **34**(4), 397–426 (2014).

[5] Z. Shen, Y. Lin, Y. Zhu, X. Liu, J. Yan, K. Yao, "Clinical comparison of patient outcomes following implantation of trifocal or bifocal intraocular lenses: a systematic review and meta-analysis," Sci. Rep. **7**(1), 45337 (2017).

[6] D. Zamora-de La Cruz, J. Bartlett, M. Gutierrez, S. M. Ng, "Trifocal intraocular lenses versus bifocal intraocular lenses after cataract extraction among participants with presbyopia," Cochrane Database Syst. Rev. **1** (2023).

[7] D. R. Breyer, H. Kaymak, T. Ax, F.T. Kretz, G. U. Auffarth, P. R. Hagen, "Multifocal intraocular lenses and extended depth of focus intraocular lenses," Asia-Pac. J. Ophthalmol. **6**, 339–349 (2017).

[8] S. N. Khonina, N. L. Kazanskiy, P. A. Khorin, M. A. Butt, "Modern types of axicons: new functions and applications," Sensors (Basel) **21**(19), 6690 (2021).

[9] W. Torres-Sepúlveda, J. F. Barrera, R. Henao, et al., "Imaging with an extended depth of field by means of the peacock eye optical element," Photon. Lett. Pol. **9**, 128–130 (2017).

[10] K. Kakarenko, I. Ducin, K. Grabowiecki, et al., "Assessment of imaging with extended depth-of-field by means of the light sword lens in terms of visual acuity scale," Biomed. Opt. Express **6**, 1738–1748 (2015).

[11] K. Petelczyc, A. Kolodziejczyk, N. Błocki, et al., "Model of the light sword intraocular lens: in-vitro comparative studies," Biomed. Opt. Express **11**(1), 40–54 (2019).

[12] W. Torres-Sepúlveda, A. Mira-Agudelo, J. F. Barrera-Ramírez, K. Petelczyc, A. Kolodziejczyk, "Optimization of the light sword lens for presbyopia correction," Transl. Vis. Sci. Technol. **9**(3), 6 (2020).

[13] Z. Jaroszewicz, A. Kołodziejczyk, D. Mouriz, J. Sochacki, "Generalized zone plates focusing light into arbitrary line segments," J. Mod. Opt. **40**(4), 601–612 (1993).

[14] A. González-Durango, "Diseño teórico de nuevos perfiles de fase asimétricos y su aplicación a sistemas ópticos," [Trabajo de grado], Antioquia, Universidad de Antioquia, Medellín, Colombia (2020).

[15] J. Armengol, N. Garzón, F. Vega, I. Altemir, M. S. Millán, "Equivalence of two optical quality metrics to predict the visual acuity of multifocal pseudophakic patients," Biomed. Opt. Express **11**(5), 2818–2829 (2020).

[16] D. Voelz, *Computational Fourier Optics: A MATLAB Tutorial*, Bellingham, SPIE Press, 113–140 (2011).

[17] F. Vega, M. S. Millán, N. Garzón, I. Altemir, F. Poyales, & J. M. Larrosa, "Visual acuity of pseudophakic patients predicted from in-vitro measurements of intraocular lenses with different design," Biomed. Opt. Express **9**(10), 4893-4906 (2018).

[18] N. Gupta, J. S. Wolffsohn, S. A. Naroo, "Optimizing measurement of subjective amplitude of accommodation with defocus curves," J. Cataract Refract. Surg. **34**(8), 1329–1338 (2008).

[19] L. Galinier, P. Renaud-Goud, J. Brusau, L. Kergadallan, J. Augereau, B. Simon, "Spiral diopter: freeform lenses with enhanced multifocal behavior," Optica **11**(2), 238–244 (2024).

1. Introduction

Presbyopia is a progressive and irreversible condition characterized by the eye's diminishing ability to focus on near objects, emerging with age. In response to this global visual challenge, decades of optical research have sought effective corrective solutions [1].

Traditional interventions include reading glasses, monovision correction (adding plus power to one eye), and multifocal designs implemented in spectacles and contact lenses. More recent attempts have aimed to restore dynamic accommodation via intraocular lenses (IOLs) or scleral expansion surgery [2-4]. Among multifocal IOLs, bifocal and trifocal variants are dominant in clinical settings [5,6]. Despite their benefits, these lenses typically provide good vision only at discrete focal distances, failing to deliver seamless visual performance across the full range of object vergences.

To overcome these limitations, extended depth-of-focus (EDOF) lenses have been introduced [7]. Unlike multifocal lenses, EDOF designs aim to create a sharp retinal image over a continuous range of object distances by smoothly varying optical power. Prominent examples of such elements include axicons [8], peacock-eye optical elements [9], and the Light Sword Lens (LSL) [10]. Previous studies on the LSL have demonstrated its efficacy in improving both near and intermediate vision based on computational, objective, and psychophysical evaluations, positioning it as a candidate for both contact and intraocular lens applications in presbyopia correction [11,12].

A foundational theory in this domain is the generalized zone plate method, introduced over three decades ago [13]. This framework enables the derivation of phase functions capable of directing incident light into line segments of arbitrary length and orientation with respect to the optical axis. Building on this concept, the present work proposes the Spiral Optical Element (SOE) [14], a novel diffractive element that divides its aperture into spiral segments. A phase function is calculated to redirect light from each subaperture to successive focal points distributed along the optical axis, forming a continuous focal line as illustrated in Figure 1a.

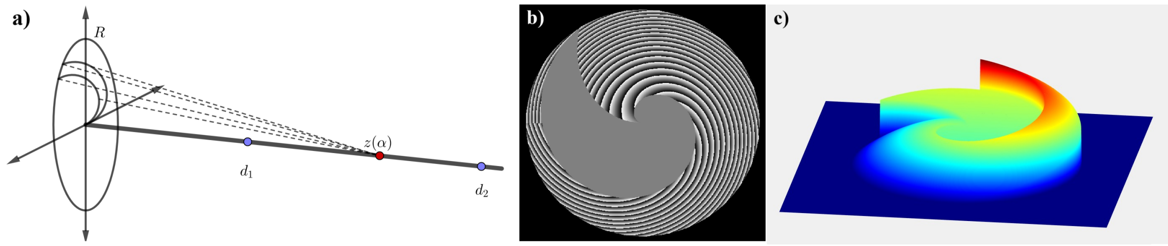

Fig. 1. a) Focusing geometry provided by the SOE b) Phase profile for the SOE for d1=45.5 cm and d2=57.5 cm and c) three-dimensional visualization of the phase profile.

This study presents a comprehensive evaluation of the SOE to assess its viability in generating extended depth-of-focus imaging and its suitability for presbyopia correction over the full functional visual range. The SOE's performance was analyzed in three stages: computational simulations, optical bench experiments, and psychophysical measurements. In the computational and experimental stages, a monofocal lens focused at infinity was compared with configurations in which the lens was compensated using either the LSL or the SOE, both modeled as contact lenses. For the psychophysical stage, comparisons were made between the naked presbyopic eye and the eye corrected with either the LSL or the SOE mimicked as contact lenses.

1.a. Theoretical construction of the element

The SOE is designed by segmenting its optical aperture into regions bounded by Archimedean spirals, mathematically defined by the equation $r = b\theta + c$, where the parameter b controls the distance between each loop and $c = 0$ is chosen to maintain the spiral's origin at the optical center. Given a circular aperture of radius a, each segment is delimited by two adjacent spirals, $r = a\theta$ and $r = \alpha\theta$, where $\alpha < a$, thus forming a subaperture through which the incident light is directed.

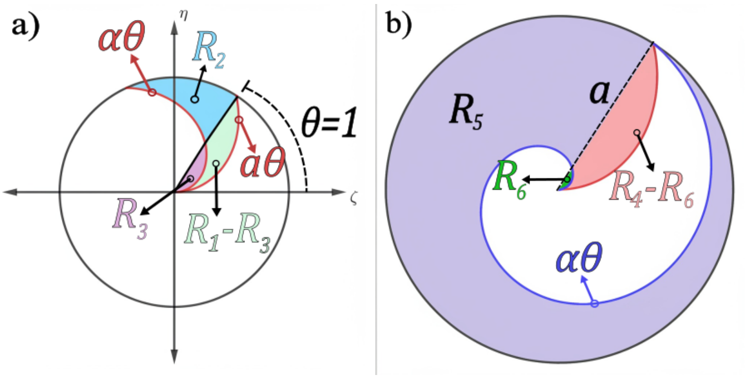

Fig. 2. Regions defined for the area calculations in a circle of radius a and the spirals a) $r = a\theta$ and $r = \alpha\theta$. b) $r = a\theta$ and $r = \frac{a}{1+2\pi}\theta$. Figure adapted from [14].

Figure 2a illustrates three fundamental regions within the aperture used for area calculations, defined as follows:

$$R_1 = \{(r, \theta): 0 < r \leq a\theta, 0 \leq \theta \leq 1\}$$

$$R_2 = \{(r, \theta): \alpha\theta \leq r \leq a, 1 \leq \theta \leq \frac{a}{\alpha}\} \quad (1)$$

$$R_3 = \{(r, \theta): 0 < r < \alpha\theta, 0 \leq \theta \leq 1\}$$

The corresponding area for each region is given by:

$$A_{R_1} = \int_0^1 \int_0^{a\theta} r\, dr\, d\theta = \frac{a^2}{6}$$

$$A_{R_2} = \int_1^{\frac{a}{\alpha}} \int_{\alpha\theta}^{a} r\, dr\, d\theta = \frac{1}{2}\left(\frac{2a^3}{3\alpha} - a^2 + \frac{\alpha^2}{3}\right) \quad (2)$$

$$A_{R_3} = \int_0^1 \int_0^{\alpha\theta} r\, dr\, d\theta = \frac{\alpha^2}{6}$$

The phase function is defined to ensure that light passing through each spiral region is directed to a unique segment along the focal line. Assuming a uniform illumination intensity K_1 across the aperture and a constant intensity K_2 along the focal line, energy conservation requires:

$$K_1(A_{R_1} + A_{R_2} - A_{R_3}) = K_2(z(\alpha) - d_1) \quad (3)$$

where d_1 and $z(\alpha)$ denote the initial and final points of the focal segment, respectively. This leads to:

$$\frac{a^3 K_1}{3\alpha} - \frac{a^2 K_1}{3} = K_2(z(\alpha) - d_1) \quad (4)$$

Following the generalized zone plate methodology presented in Ref. [13], the analysis starts with a single partition (only one subaperture) and is then extended across the full aperture to determine the d_2 extreme of the focal segment. In the SOE's case, the spiral segment with the greatest covered area without overlapping is used as the base unit, as defined by: $r = \frac{a}{1+2\pi}\theta$ (see Figure 2b).

The area enclosed between the circle of radius a and the spirals $a\theta$ and $\frac{a}{1+2\pi}\theta$ is calculated by defining the regions (5), as shown in Figure 2b.

$$R_4 = \{(r,\theta): 0 < r \leq a\theta, 0 \leq \theta \leq 1\}$$
$$R_5 = \left\{(r,\theta): \frac{a}{1+2\pi}\theta \leq r \leq a, 1 \leq \theta \leq 1+2\pi\right\} \quad (5)$$
$$R_6 = \left\{(r,\theta): 0 < r < \frac{a}{1+2\pi}\theta, 0 \leq \theta \leq 1\right\}$$

Any remaining portion of the aperture not included in the spiral configuration is left unmodulated, corresponding to zero optical power (i.e., a phase value of zero) and given by the region:

$$R_0 = \{(r,\theta) \mid 0 \leq r \leq a, 0 \leq \theta < 2\pi, r \leq r_2(\theta)\} \cup \{(r,\theta) \mid 0 \leq \theta \leq 1, r_1(\theta) \leq r \leq r_2(\theta+2\pi)\} \quad (6)$$

Where $r_1(\theta) = a\theta, r_2(\theta) = \frac{a}{1+2\pi}\theta$ and $0 \leq r \leq a, 0 \leq \theta < 2\pi$.

The area values of regions (5) are given by:

$$A_{R_4} = \int_0^1 \int_0^{a\theta} r\, dr\, d\theta = \frac{a^2}{6}$$
$$A_{R_5} = \int_1^{1+2\pi} \int_{\frac{a}{1+2\pi}\theta}^{a} r\, dr\, d\theta = \frac{a^2}{2}\left(\frac{2(1+2\pi)}{3} + \frac{1}{3(1+2\pi)^2} - 1\right) \quad (7)$$
$$A_{R_6} = \int_0^1 \int_0^{\frac{a}{1+2\pi}\theta} r\, dr\, d\theta = \frac{1}{6}\left(\frac{a}{1+2\pi}\right)^2$$

Substituting regions (7) in (3) and replacing $z(\alpha)$ with d_2, since the full aperture will focus light on the line defined by $d_2 - d_1$, yields:

$$\frac{a^2K_1}{6} + \frac{2a^2K_1(1+2\pi)}{6} + \frac{a^2K_1}{6(1+2\pi)^2} - \frac{a^2K_1}{2} - \frac{K_1}{6}\left(\frac{a}{1+2\pi}\right)^2 = K_2(d_2 - d_1)$$
$$\frac{a^2K_1}{6} + \frac{a^2K_1(1+2\pi)}{3} - \frac{a^2K_1}{2} = K_2(d_2 - d_1) \quad (8)$$
$$\frac{a^2K_1(1+2\pi)}{3} - \frac{a^2K_1}{3} = K_2(d_2 - d_1)$$
$$\frac{2\pi a^2K_1}{3(d_2 - d_1)} = K_2$$

By combining equations (4) and (8) and expressing the focal position z as a function of α, the relation between the phase profile to the focal segment is obtained in (9).

$$z(\alpha) = \frac{(d_2 - d_1)}{2\pi}\left(\frac{a}{\alpha} - 1\right) + d_1 \quad (9)$$

Substituting the Archimedean spiral equation $\alpha = \frac{r}{\theta}$ on equation (9) derives the function that identifies each point (r,θ) on the aperture of the element, where light passes through, to its corresponding distance $z(r,\theta)$ along the optical axis, where light will be focused.

$$z(r,\theta) = \frac{(d_2 - d_1)}{2\pi}\left(\frac{a\theta}{r} - 1\right) + d_1 \tag{10}$$

The resulting phase profile is governed by a ray-tracing differential equation, as found in [14].

$$\frac{\partial\, \varphi(\zeta,\eta)}{\partial\, \zeta} = \frac{x - \zeta}{d}$$
$$\frac{\partial\varphi(\zeta,\eta)}{\partial\eta} = \frac{y - \eta}{d} \tag{11}$$

It is necessary to perform a coordinate transformation into polar coordinates for our problem at hand using the chain rule, yielding the following equations:

$$\frac{\partial\varphi(r\cos\theta, r\sin\theta)}{\partial r} = \frac{\partial\varphi(\zeta,\eta)}{\partial\zeta}\cos\theta + \frac{\partial\varphi(\zeta,\eta)}{\partial\eta}\sin\theta$$
$$\frac{\partial\varphi(r\cos\theta, r\sin\theta)}{\partial\theta} = -\frac{\partial\varphi(\zeta,\eta)}{\partial\zeta}r\sin\theta + \frac{\partial\varphi(\zeta,\eta)}{\partial\eta}r\cos\theta \tag{12}$$

Using the coordinate change definition $\zeta = r\cos\theta$and $\eta = r\sin\theta$, and given that $|\ \zeta\ | \ll 1$and $|\ \eta\ | \ll 1$ for paraxial approximation, substituting (11) into equations (12), and given that d is the distance from the optical element to each point of the focal segment, it can be denoted as $z(r,\theta)$.

$$\frac{\partial\varphi(r\cos\theta, r\sin\theta)}{\partial r} = \frac{x - r\cos\theta}{z(r,\theta)}\cos\theta + \frac{y - r\sin\theta}{z(r,\theta)}\sin\theta = \frac{x\cos\theta - r\cos^2\theta + y\sin\theta - r\sin^2\theta}{z(r,\theta)}$$
$$\frac{\partial\varphi(r\cos\theta, r\sin\theta)}{\partial\theta} = -\frac{x - r\cos\theta}{z(r,\theta)}r\sin\theta + \frac{y - r\sin\theta}{z(r,\theta)}r\cos\theta = \frac{-xr\sin\theta + r^2\cos\theta\sin\theta + yr\cos\theta - r^2\sin\theta\cos\theta}{z(r,\theta)} \tag{13}$$

Further simplifying equations (13) results in the transformations of the paraxial ray-tracing equations from Cartesian to polar coordinates.

$$\frac{\partial\phi}{\partial r} = \frac{x cos\theta + y sin\theta - r}{z(r,\theta)}$$
$$\frac{\partial\phi}{\partial\theta} = \frac{x r sin\theta + y r cos\theta}{z(r,\theta)} \tag{14}$$

Assuming the focal line is aligned with the optical axis (x = y = 0), and substituting equation (10) in (14):

$$\frac{\partial\phi}{\partial r} = \frac{-r}{\frac{(d_2 - d_1)}{2\pi}\left(\frac{a\theta}{r} - 1\right) + d_1} \tag{15}$$

Integrating (15) leads to the SOE's phase function:

$$\begin{cases} \phi(r,\theta)=0, \text{if } (r,\theta)\in R_0 \\ \phi(r,\theta)=\dfrac{-2\pi}{B^3}\left(A^2\ln|A+Br|-\dfrac{3}{2}A^2+\dfrac{B^2r^2}{2}-ABr\right), otherwise \end{cases} \quad (16)$$

Where $A=(d_2-d_1)a\theta$ and $B=2\pi d_1-(d_2-d_1)$. Here, d_2-d_1 corresponds to the DOF of the SOE and a to the pupil radius of the element.

Within the framework used to construct the phase profile under paraxial approximation, a spiral phase element is theoretically expected to focus a plane wave at continuous points along the optical axis. However, as noted in equation (16), the phase function derived from energy conservation principles exhibits an inherent inconsistency with the azimuthal invariance condition ($\partial\varphi/\partial\theta=0$). This mathematical discrepancy indicates that axial focusing by the SOE is fundamentally approximate rather than exact. The implications of this theoretical limitation warrant careful examination: if perfect point focusing cannot be achieved, the question arises as to what focal structure actually emerges and whether this approximation compromises the element's optical functionality. To address this concern, a comprehensive three-dimensional numerical analysis of the point spread function (3D) across the design range is presented in Section 3.

2. Methodology

As a preliminary step, computational simulations were carried out to evaluate the SOE's optical performance across different focal line lengths and distances. The goal was to identify an optimal design for intermediate vision, centered around −2.00 D, and a depth of focus comparable to the one exhibited by the LSL. The best-performing design out of 20 different configuration was achieved with parameters $d_1=45.5$ cm and $d_2=57.5$ cm, producing a theoretical depth of focus (DOF) of 0.45 D. The phase profile of this configuration is shown in Figure 1b, codified in modulo 2π to be displayed in a spatial light modulator, and its three-dimensional reconstruction is shown in Figure 1c. For comparative purposes, the LSL was configured to provide optical power from 0.00 D to −3.00 D. Both optical elements were simulated using a 5.00 mm pupil diameter.

To examine the actual focal structure produced by the spiral geometry, a comprehensive three-dimensional Point Spread Function (PSF) analysis was performed. As illustrated schematically in Figure 1a, the propagation of light through the SOE was simulated across the design range, tracing how the spiral phase profile directs incoming plane waves along the optical axis. 101 PSF calculations were computed at equally spaced distances spanning 40.0–62.1 cm (corresponding to object vergences from –2.50 to –1.61 D. For each distance plane, the complex amplitude distribution was calculated by propagating the field immediately after the SOE using Fraunhofer diffraction theory, accounting for the full spiral phase modulation pattern. The resulting PSF intensity distributions were then assembled into a volumetric dataset in the ImageJ FIJI software, enabling visualization of the complete focal structure.

All simulations and performance analyses were conducted using MATLAB® R2022b. For each lens configuration (monofocal, LSL, and SOE), the point spread function (PSF) and modulation transfer function (MTF) were computed using a wavelength of 555 nm. The area under the MTF curve (MTFa) was used as the quality metric, as it closely correlates with visual acuity (VA) in real-eye conditions [15]. Object vergences ranged from −4.00 D to +1.00 D in increments of 0.25 D. Additionally, the expected retinal images were generated using a convolution model with spatially incoherent light [16] and a Snellen optotype "E" as the object.

The experimental evaluation employed a monocular visual simulator (MVS), similar to the system described in Ref. [12] (see Figure 3). The MVS included a spatial light modulator (SLM), Hartmann–Shack wavefront sensor (HSS), artificial pupil (Pup), electro-optical lens (EOL), and a polychromatic stimulus pathway. Phase profiles were projected onto the SLM an LCoS (liquid crystal on silicon) modulator, phase-only, model PLUTO-NIR, Holoeye Photonics AG, Germany), with a resolution of 1920 × 1080 pixels and a pixel size of 8 μm. The SLM was calibrated for a wavelength of 532 nm in the angular range $[0,2\pi]$. Images of Snellen optotype were captured using a CMOS camera (Basler acA2040-55uc) coupled with an imaging lens. Object vergence levels varied from −4.00 D to +1.00 D in 0.25 D steps, induced via the EOL (Optotune EL-16-40-TC-VIS-20D).

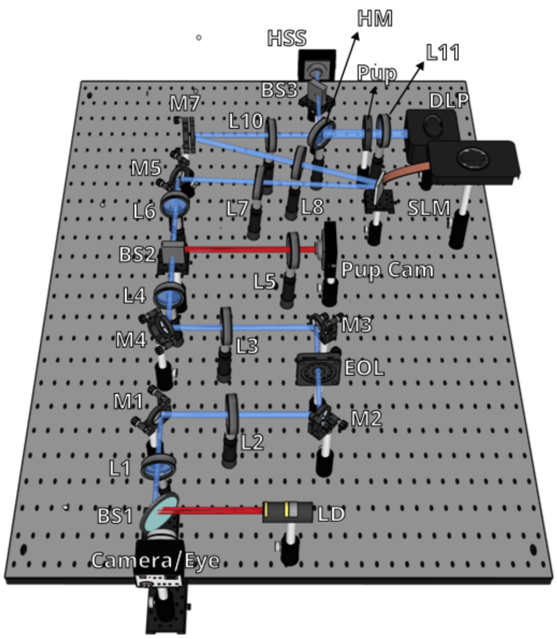

Fig. 3. Diagram of the monocular visual simulator used for experimental recording of Snellen optotype images and measurements of visual acuity in both the naked and compensated presbyopic eye. L: lens; BS: Beam Splitter; M: mirror; EOL: Electro-Optical Lens; LD: Laser Diode: HM: Heat Mirror; SLM: Spatial Light Modulator; Pup Cam: Camera, Pup: artificial pupil. DLP: Digital Light Processing projector. HSS: Hartmann-Shack Sensor

Five participants aged 21 to 34 years (mean: 25 years) took part in the psychophysical testing. Presbyopia was pharmacologically simulated in each subject by paralyzing the ciliary muscle with a topical muscarinic antagonist. Testing was conducted in each participant's dominant eye, determined by sighting dominance. Refractive errors ranged from −2.75 D to 0.15 D (mean = −1.18 D, SD = 1.24 D), while astigmatism values ranged from −1.72 D to −0.67 D (mean = −1.19D, SD = 0.44 D), measured using the HSS and the laser diode of the system. Visual Acuity was evaluated for a set of defocus induced with the EOL relative to the subject's best subjective focus: −4, −3, −2, −1, −0.5, 0, +1 D.

Visual acuity through-focus curves were obtained under three conditions: naked eye, eye corrected with the LSL, and eye corrected with the SOE. The same object vergence range used in the optical bench experiment was applied. Further procedural details can be found in Ref. [12]. All procedures adhered to the principles of the Declaration of Helsinki and were approved by the Bioethics Committee of the University Research Center (SIU) at the University of Antioquia

3. Results & Discussion

The 3D visualization of the SOE's focal structure in Figure 4 reveals the spiral geometry creates an inherently asymmetric element that deviates from the azimuthal invariance condition required for exact axial focusing. This asymmetry implies that different azimuthal sectors of the spiral contribute focusing power at different off-axis positions. However, the reconstruction demonstrates that despite this asymmetric architecture, the focal structure remains predominantly concentrated along the optical axis throughout the evaluated range, with maximum intensity localization observable at the central region, corresponding to –2.00 D.

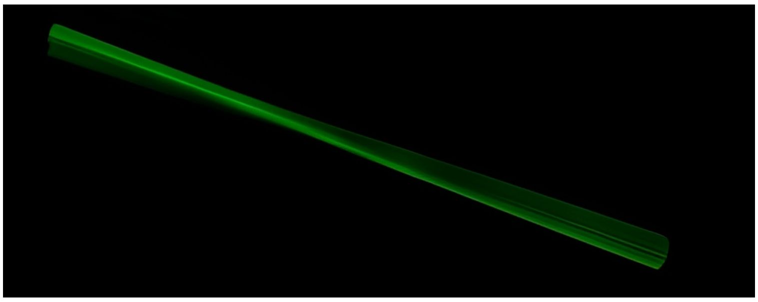

Fig. 4. Three-dimensional reconstruction of the SOE's point spread function from −2.50 D to −1.50 D, showing the extended focal distribution along the optical axis.

The optical performance of each element was quantified using MTFa curves for spatial frequencies ranging from 0.00 to 50.0-line pairs per millimeter (lp/mm), under 555 nm spatially incoherent illumination and a 5.00 mm pupil diameter. The spatial frequency range in image space was defined according to ISO 11979-2 standard recommendations for intraocular lens testing, which specifies evaluation up to 50 lp/mm at the image plane of a model eye with standardized optical parameters, as utilized in [17]. Figure 5 presents these results. As expected, the monofocal system exhibited a sharp decline in image quality with increasing defocus. The LSL maintained relatively uniform performance throughout its design range [12]. The SOE showed two pronounced peaks—one at 0.00 D (attributable to the non-modulated region) and another near −2.00 D—consistent with the element's theoretically designed profile. These findings provide strong preliminary evidence supporting the SOE's suitability for extended depth of focus imaging.

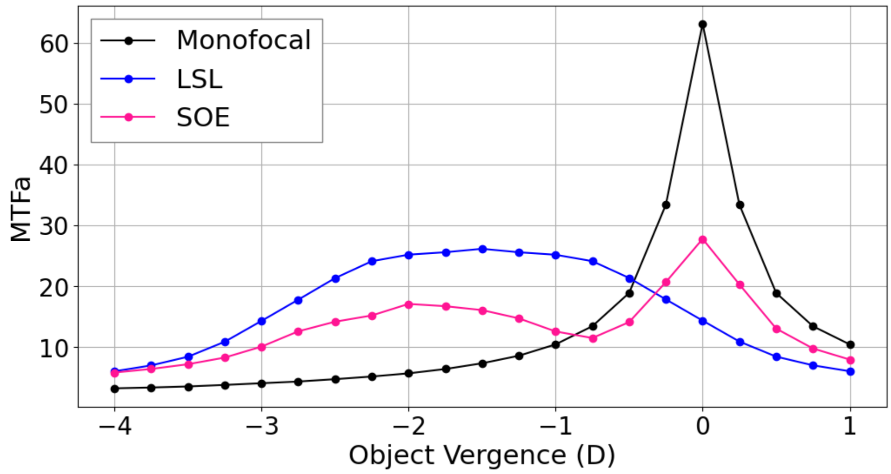

Fig. 5. MTFa curves as a function of defocus for a 5 mm pupil diameter. Monofocal: black line; LSL: blue line; SOE: red line.

Table 1 compares simulated and experimental Snellen optotype images generated by the monofocal lens and with LSL and SOE corrections, across selected object vergence levels. As expected, image quality from the monofocal system degraded with increased defocus. The LSL maintained consistent structural fidelity across its operational range. The SOE performed optimally around −2.00 D and exhibited superior image quality over a broader range than the monofocal system, though not as consistently as the LSL. Notably, there was good agreement between the simulated and experimental images across all three systems.

Table 1: Simulated (left) and experimental (right) Snellen images with monofocal, LSL, and SOE at varying object vergences.

	Simulated Images			**Experimental Images**		
	Monofocal	**LSL**	**SOE**	**Monofocal**	**LSL**	**SOE**
0D	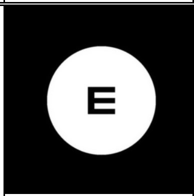	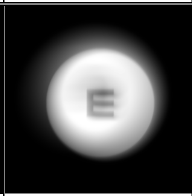	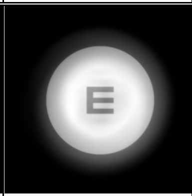	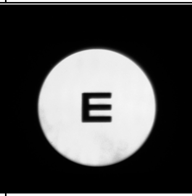	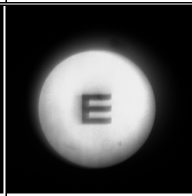	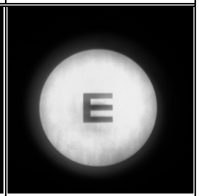
-1D	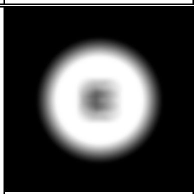	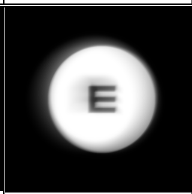	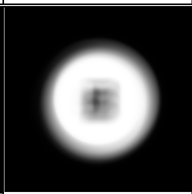		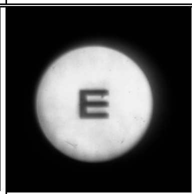	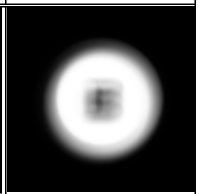
-1.5D	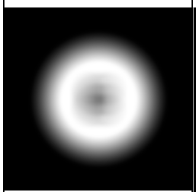	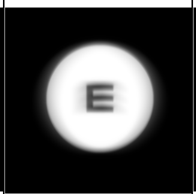	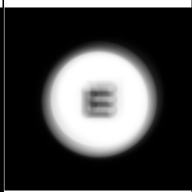	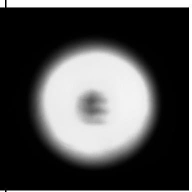	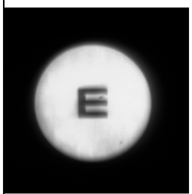	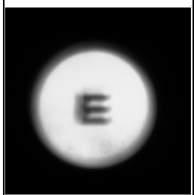
-2D	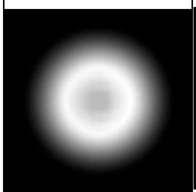	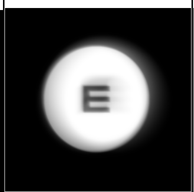	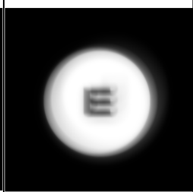	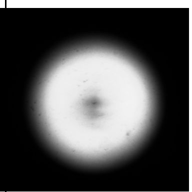	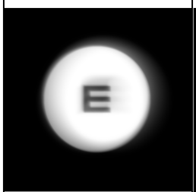	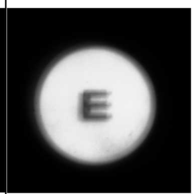
-3D	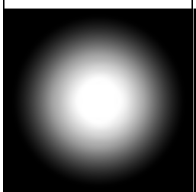	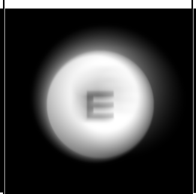	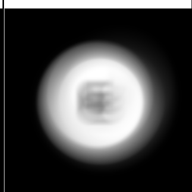	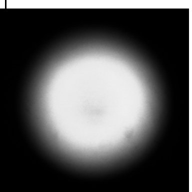	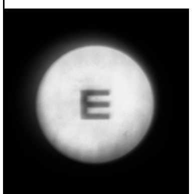	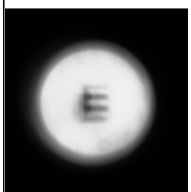
-4D	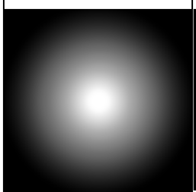	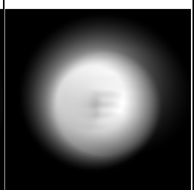	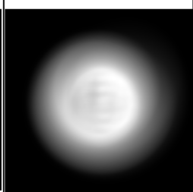	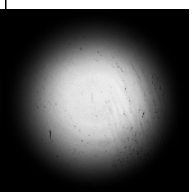	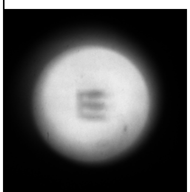	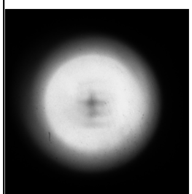

To provide an objective comparison of the images presented in Table 1, the correlation coefficient (CC) was calculated using the monofocal lens images at target vergence of 0.00 D as reference. Figure 6a displays the CC curves for the three computationally simulated optical systems, showing a consistent behavior with the trends observed in Figure 5. The CC values exhibited by the SOE at −2.00 D and 0.00 D achieve peak values comparable to those of the LSL. Outside the design range, image quality degradation is observed for the SOE, though this decline is less pronounced than suggested by the SRMTF results in Figure 5. Figure 6b presents analogous results obtained from experimental images captured with the model visual system (MVS). The primary difference lies in the SOE's lower CC values relative to the LSL, indicating overall reduced correlation in the experimental setting.

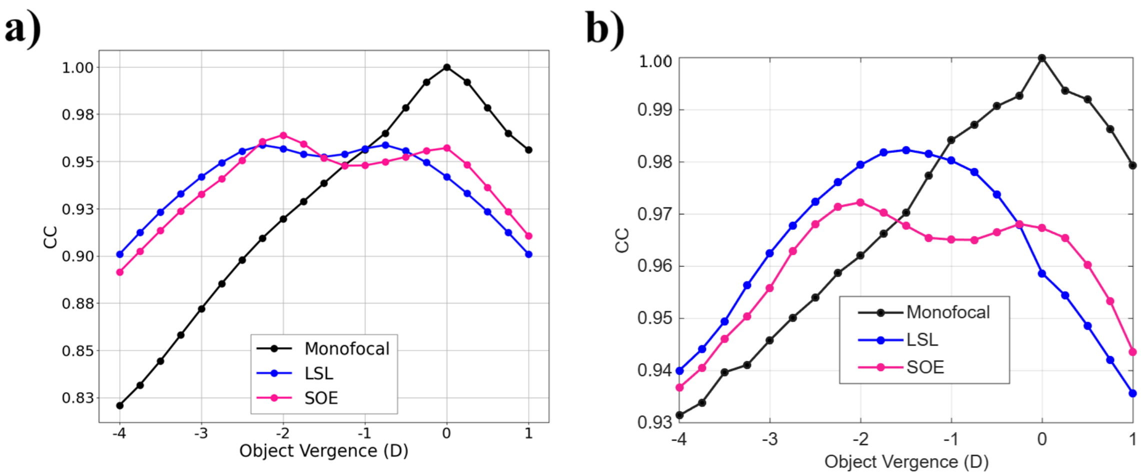

Fig. 6. Correlation Coefficient (CC) as a function of defocus for a 5 mm pupil diameter. Monofocal: black line; LSL: blue line; SOE: red line obtained by a) computational simulations and b) optical bench experiment in the MVS.

Figure 7 shows the mean VA curves obtained from the five participants. The best corrected distance visual acuity for the naked eye occurred at 0.00 D (0.02 ± 0.09 in a logMAR scale), with VA rapidly declining at other object vergences, reaching a value (in logMAR scale) of 0.94 ± 0.08 at -4 D. The LSL correction yielded a relatively flat VA profile from -3.00 D to 0.00 D, in agreement with its designed optical power range, with an average VA value of 0.13 in logMAR scale in this object vergence range. As can be observed, the VA values and their error bars overlap within this defocus range, indicating statistical equivalence. The SOE, in contrast, exhibited a dual-peak response at object vergences 0.00 D and -2.00 D, providing effective compensation at both near (-2 D, VA value 0.12 ± 0.04 in logMAR scale) and far (0 D, VA value 0.11 ± 0.09 in logMAR scale) distances. The VA values at these defocus levels are statistically indistinguishable for SOE and LSL, indicating that both diffractive elements perform in a similar way. However, the quasi-constant behavior of the LSL endows it with more favorable features for presbyopia compensation. Despite this, the dual-peak behavior of the SOE was consistent across simulations, optical bench testing, and human trials, confirming the robustness of the SOE against individual ocular aberrations and its clear superiority over the naked presbyopic eye when no corrections were applied. Nevertheless, it is necessary to optimize the phase profile of the SOE in order to improve its performance in distance vision, an important requirement for any element designed to correct presbyopia.

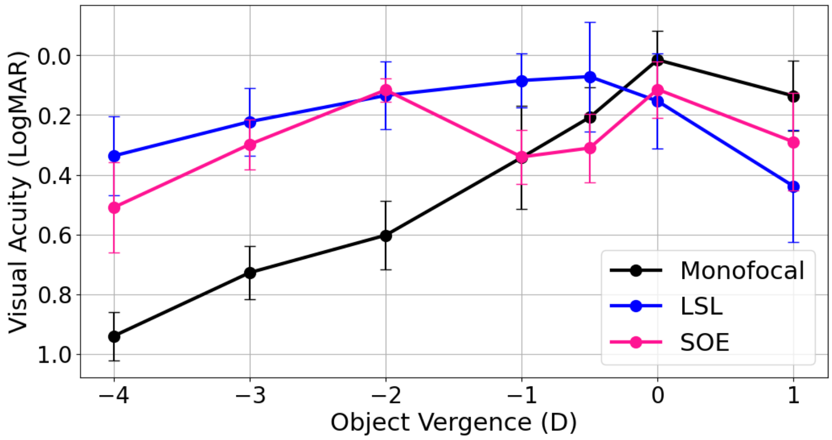

Fig. 7. Through-focus mean visual acuity (VA) for the naked eye (black), and the eye corrected with the LSL (blue) and the SOE (red).

To quantify depth of focus (DOF) all previous results were used, defining DOF as the object vergence range where image quality remained above 80% of the peak value [18]. Since the data was obtained at discrete points, we applied interpolation to estimate DOF. Results are shown in Table 2.

Table 2. Depth of focus in diopters (D) derived from MTFa, simulated and experimental CC and logMAR VA data.

Metric	**Monofocal**	**LSL**	**SOE**
MTFa	0.13	1.88	0.92
CC sim	0.77	2.61	1.08
CC exp	0.62	1.89	1.34
LogAV	0.24	2.12	0.98

Overall, a strong agreement was observed between computational and experimental results across all optical systems. The LSL demonstrated the highest performance across all metrics, substantially exceeding those of the monofocal lens, while SOE yielded intermediate values, representing considerable improvement over the monofocal system while remaining below LSL performance levels. Interestingly, the naked eye (monofocal) condition exhibited greater tolerance to defocus in experimental measurements than computational predictions would suggest. This discrepancy likely reflects neural compensation mechanisms that partially mitigate the effects of optical defocus in human visual perception. Conversely, the computational simulations slightly overestimated depth of focus for both EDOF designs. Notably, the SOE exhibited the smallest discrepancy between predicted and measured performance, highlighting its optical stability.

Recently, another diffractive optical element with spiral focusing geometry has been proposed [19], named Spiral Diopter, having among its possible applications the correction of presbyopia. However, it is worth noting that its design is fundamentally different from the element presented in this work. The spiral diopter's focusing geometry is based on Fermat spirals, with the goal of being a multifocal element (discrete number of foci), not an element with EDOF based on the Arquimedes' spiral as the SOE. While the multifocal characteristic could be crucial in miniaturizing emerging technologies while retaining their optical quality, the EDOF technology is still a superior option for presbyopia correction, as it can bridge the shortcomings between monofocal and multifocal lens.

4. Conclusions

The Spiral Optical Element (SOE) demonstrated reliable and consistent performance across three evaluation stages: computational modeling, optical bench testing, and psychophysical trials. In each case, the SOE produced image quality patterns aligned with its theoretical design, including the dual-peak visual acuity response. The experimental data further suggests that individual ocular aberrations did not significantly impair the SOE's functionality, reinforcing the robustness of its design. However, a more detailed investigation is warranted to assess the potential impact of subject-specific higher-order aberrations on SOE performance.

Despite the limited sample size, the results suggest that the SOE is a promising candidate for presbyopia correction. It effectively provides compensation for both near and far vision, maintaining distance clarity more effectively than the LSL, which typically prioritizes near-to-intermediate performance at the expense of distance vision.

To further enhance the SOE's optical performance—particularly, its depth of focus—it may be advantageous to incorporate targeted aberration terms into its phase function. Specifically, the currently unused central region of the phase profile (see Figure 1b) offers an opportunity for refinement, potentially allowing for aspheric-like corrections that could extend its application both in presbyopia correction and broader EDOF optical systems.

Acknowledgements

This research was supported by the Comité para el Desarrollo de la Investigación-CODI (Universidad de Antioquia UdeA, Colombia) under the Programmatic Call for Exact and Natural Sciences 2022-2023. Walter Torres-Sepúlveda also acknowledges support from the Fondo Francisco José de Caldas (Colciencias-Colombia, grants 727 of 2015), and the support from the Institución Universitaria Digital de Antioquia under the project No. 2023059927005 titled "Implementación de técnicas de inteligencia artificial para el sensado experimental de aberraciones ópticas mediante el análisis de patrones de Speckle."